Chinese Chemical Letters 37 (2026) 112114

Contents lists available at ScienceDirect

Chinese Chemical Letters

journal homepage: www.elsevier.com/locate/cclet

Entropy-stabilized nanoporous structures enable sintering-resistant Pt species

Yunpeng Wang[1], Zhuxin Lyu[1], Yueming Sun, Yunqian Dai*

School of Chemistry and Chemical Engineering, Southeast University, Nanjing 211189, China

ARTICLE INFO

Article history:
Received 30 June 2025
Revised 13 November 2025
Accepted 13 November 2025
Available online 14 November 2025

Keywords:
Porous
Nanofibers
High entropy
Pt
CO oxidation

ABSTRACT

Supported noble-metal catalysts often suffer from nanoparticle sintering, resulting in rapid deactivation under high-temperature conditions. We report hierarchically porous spinel type high-entropy oxide (S-HEO) nanofibers, $(CrMnFeCoMg)_3O_4$, as robust supports for Pt nanoparticles. The porous structure (38.5 m^2/g) endows thermal stability, preserving porosity after 880 °C calcination. The porous Pt/S-HEO-500 exhibits exceptional sinter-resistance. Under 500 °C calcination, Pt exhibits only a 0.2 nm growth increment, owing to the physical confinement and strong metal–support interactions. For Pt/S-HEO-500, the T_{50} (50 % conversion temperature) for CO oxidation was merely 9 °C higher than that without calcination, with 100 % conversion retained over 100 h of steady-state operation. These findings position porous spinel HEO nanofibers as a versatile platform for designing sinter-resistant noble-metal catalysts in high-temperature applications.

© 2025 Published by Elsevier B.V. on behalf of Chinese Chemical Society and Institute of Materia Medica, Chinese Academy of Medical Sciences.

In recent decades, nanocatalyst advances have enabled precise control over surfaces and interfaces in heterogeneous systems, establishing foundations for optimized environmental and energy applications [1,2]. However, metal sintering critically impairs catalyst activity and long-term stability. The nanoporous structure of catalyst supports dictates key properties like surface area and pore volume and plays a critical role in catalytic activity and stability [3–5]. However, conventional oxide supports (*e.g.*, CeO_2, TiO_2) suffer from pore collapse and crystallite growth under thermal stress, leading to catastrophic sintering of active components and rapid performance degradation [6–8]. This structural instability under high-temperature operation remains a fundamental bottleneck in heterogeneous catalysis.

Since 2015, high-entropy oxides (HEOs) represent an emerging class of metal oxides characterized by a near-equimolar distribution of five or more metallic elements within a single-phase lattice, resulting in atomic-level cation disorder [9–11]. HEOs achieve a significant enhancement in the thermal stability of the material through the atomic-level disordering of five or more equivalent-molar metals, utilizing the configurational entropy effect ($\Delta S_{conf} \geq$ 1.5 R) [12–14]. HEOs further exhibit multi-electron redox capabilities, positioning them as promising platforms for stabilizing metal species. Conventional synthesis techniques, such as ball milling, offer limited control over the nanoscale architecture of HEOs [15,16]. Electrospinning offers a versatile and scalable route to fabricate ultrafine HEO nanofibers, overcoming limitations of conventional methods [17]. This technique bridges the gap between atomically engineered powders and functional advanced materials, holding great potential for next-generation catalytic systems. Such entropy-stabilized porous architectures demonstrate exceptional promise in energy conversion and environmental catalysis [18,19].

We developed an electrospinning-derived strategy to fabricate spinel type $(CrMnFeCoMg)_3O_4$ high-entropy oxide (S-HEO) nanofibers, exhibiting thermally robust pore structures under thermal stress. Through systematic design and structural optimization, the configurational entropy was enhanced to 1.61 R, thus enabling the S-HEO nanofibers to retain their nanoporous structure following aging at 880 °C. The physical confinement brought by the slow diffusion effect of high-entropy oxides effectively stabilized the Pt nanoparticles, thereby achieving the sinter-resistance of the Pt/S-HEO. After being aging in an air atmosphere at 500 °C, the size of Pt nanoparticles only increased by 0.2 nm. Remarkably, Pt/S-HEO-500 exhibited a T_{50} (50 % CO conversion temperature) merely 9 °C above its uncalcined counterpart, with >100 h stability in continuous CO oxidation. Remarkably, Pt/S-HEO-500 catalyst exhibited minimal activity loss after 47 h of continuous operation at ~59 % CO conversion, with a deactivation rate constant of 6.5×10^{-3} h^{-1}. This entropy-engineering approach establishes a

* Corresponding author.
E-mail address: daiy@seu.edu.cn (Y. Dai).
[1] These authors contributed equally to this work.

https://doi.org/10.1016/j.cclet.2025.112114
1001-8417/© 2025 Published by Elsevier B.V. on behalf of Chinese Chemical Society and Institute of Materia Medica, Chinese Academy of Medical Sciences.

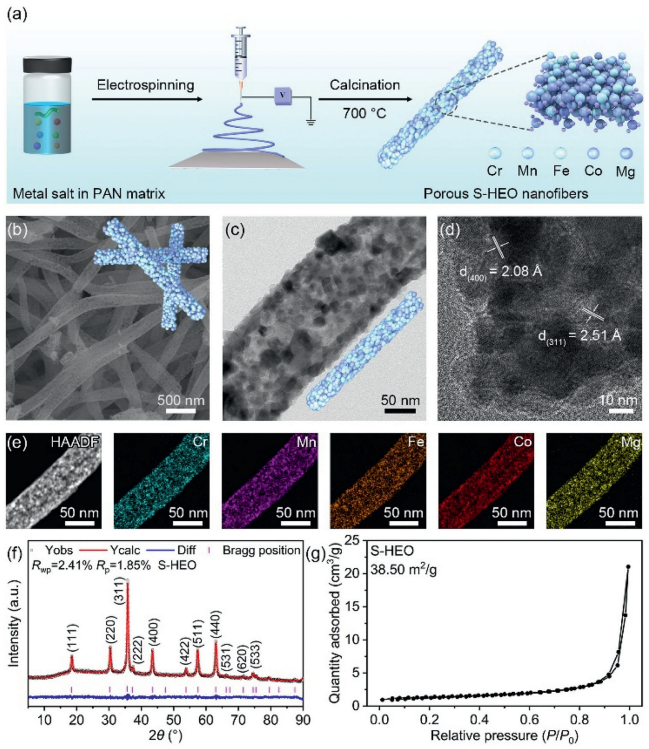


Fig. 1. (a) Schematic illustration for electrospinning S-HEO nanofibers. (b) SEM, (c) TEM, (d) HRTEM, and (e) HAADF–STEM and elemental mapping images of S-HEO nanofibers. The scale bars in (e) are 50 nm. (f) XRD patterns of HEO nanofibers. Rietveld refinement shows data points (red circle), the calculated intensity (black line), the positions of reflection peaks (pink vertical bar), and the difference profile (blue line). (g) N_2 adsorption/desorption isotherms of the HEO nanofibers.

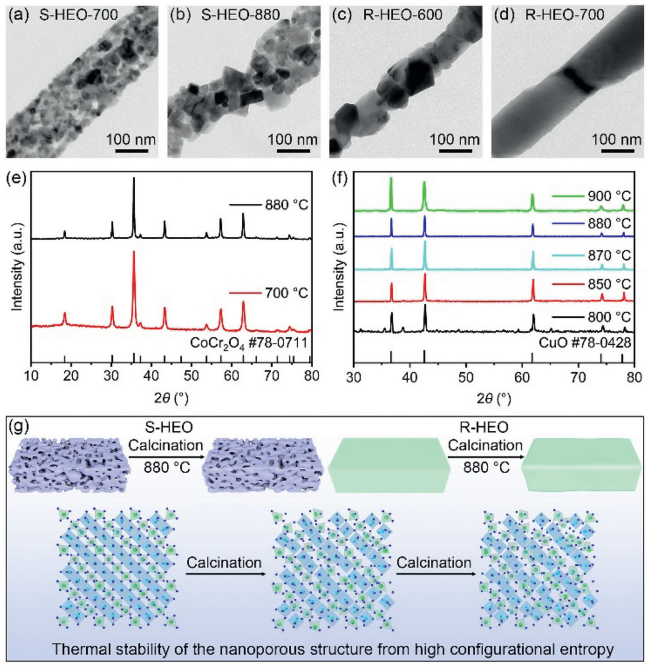


Fig. 2. (a, b) TEM images of S-HEO nanofibers at elevated temperatures. (c, d) TEM images of R-HEO nanofibers at elevated temperatures. (e) XRD patterns of S-HEO nanofibers at elevated temperatures. (f) XRD patterns of R-HEO nanofibers at elevated temperatures. (g) Schematic illustration for the thermal stabilization mechanism of pore structures of S-HEO nanofibers.

universal paradigm for sintering-resistant catalyst design, with transformative implications for industrial catalysis and energy conversion technologies.

The porous S-HEO nanofibers were synthesized *via* electrospinning, followed by calcination at 700 °C (Fig. 1a). As shown in Fig. 1b, SEM analysis reveals that the porous nanofibers possess a uniform morphology with an average diameter of 131 nm (Fig. S1 in Supporting information). The TEM image reveals the nanoporous structure and homogeneity of the nanofibers (Fig. 1c). As shown in the HRTEM image (Fig. 1d), HEO exhibits lattice distances of 2.08 and 2.51 Å, which correspond to the (400) and (311) planes of spinel-type oxides, respectively. The high-angle annular dark-field scanning transmission electron microscopy (HAADF–STEM) and elemental mapping of Cr, Mn, Fe, Co, Mg, and O confirms their homogeneous distribution throughout the nanofibers, with the metal cations exhibiting an almost equimolar ratio of 1:1:1:1:1 (Fig. 1e and Fig. S2 in Supporting information).

XRD (Fig. 1f) confirms the phase-pure spinel structure of $(CrMnFeCoMg)_3O_4$ nanofibers, exhibiting diffraction peaks at 18.41°, 30.29°, 35.68°, and 43.36° reflections at the (111), (220), (311), and (222) planes (JCPDS No. 78–0711, $CoCr_2O_4$). Using the Scherrer equation, the average crystallite size of the sample calcined at 700 °C was determined to be 16.7 nm, in excellent agreement with TEM observations. Rietveld refinement produced $R_{wp} = 2.41\,\%$ and $R_p = 1.85\,\%$, both well below the 5% threshold, confirming a high degree of agreement between the structural model and the experimental data [20]. The refined lattice parameter $a = 8.356$ Å is slightly expanded relative to the conventional spinel value (~8.34 Å), attributable to the incorporation of larger-radius cations (*e.g.*, Mg^{2+}: 0.72 Å; Fe^{3+}: 0.64 Å). This evidence proves the fabrication of HEO nanofibers.

The Brunauer–Emmett–Teller specific surface area of the spinel-type high-entropy oxide nanofibers reaches 38.5 m^2/g (Fig. 1g), significantly surpassing that of conventional HEO reported in the literature, and thus providing an ideal platform for catalysis. The hysteresis diffusion effect of high-entropy oxides is conducive to stabilizing the pore structure, rendering these oxides excellent supports for metal nanoparticles under harsh conditions [21–23].

The $(MgCoNiCuZn)_{0.2}O$ (R-HEO) nanofibers were fabricated via electrospinning and subsequent calcination in air at 880 °C. SEM demonstrates that the coral-like nanofibers exhibit a highly uniform structure, with an average diameter of 158 nm (Figs. S3 and S4 in Supporting information). TEM and HAADF–STEM combined with elemental mapping revealed nanoscale uniformity in the distribution of Cr, Mn, Fe, Co, Zn, and O throughout the nanofibers (the Cu signal enhancement originates from the TEM copper grid background). This compositional homogeneity aligns with the stoichiometric design of high-entropy oxides and confirms successful HEO synthesis (Figs. S5 and S6 in Supporting information). However, the specific surface area of the R-HEO is 2.25 m^2/g, directly correlated with its densely packed architecture (Fig. S7 in Supporting information).

Experimental results demonstrate that the S-HEO fibers maintain an intact porous morphology after high-temperature aging at 700 °C, and even at 880 °C the pore channels remain clearly visible (Figs. 2a and b). S-HEO attains a single-phase spinel structure as early as 700 °C, and the resultant slow diffusion effect inherent to the high-entropy lattice markedly inhibits grain growth and fusion (Fig. 2e).

In stark contrast, the R-HEO nanofibers lose their nanoporous architecture completely at 600 °C and above, retaining only their macroscopic nanofiber geometry (Figs. 2c and d). At 800 °C, the XRD pattern exhibits coexisting reflections attributable to Co_3O_4 (JCPDS No. 73–1701) and ZnO (JCPDS No. 76–0704), indicating that the material has not yet formed a single rock-salt phase and that a portion of the Cu remains unincorporated into the solid solu-

tion. Upon raising the temperature to 880 °C, the diffraction pattern undergoes a marked transformation: new peaks emerge at 36.6°, 42.6°, 61.8°, 74.0°, and 77.9°, which are indexed to the (111), (200), (220), (311), and (222) planes of a face-centered cubic structure (JCPDS No. 78–0428), in full agreement with a rock-salt lattice. This confirms that all five metal cations have achieved atomic-level mixing to form a single-phase high-entropy oxide. Importantly, elevating the calcination temperature to 900 °C results in the re-emergence of CuO and Cu_2O reflections (JCPDS No. 78–2076) in the XRD pattern, indicating the incipient phase separation of copper under such extreme thermal conditions (Fig. 2f). Concurrent lattice-parameter analysis reveals a systematic shift of the principal diffraction peaks toward lower angles as the temperature rises from 800 °C to 880 °C. This peak shift, indicative of lattice expansion, is attributed to the substitution of smaller-radius cations by larger-radius species at elevated temperatures, resulting in increased overall lattice distortion [24].

This pronounced difference arises from their compositional designs. The high configurational entropy promotes the formation of high-entropy oxides, which exhibit the slow diffusion effect that significantly reduces atomic migration rates, thereby enhancing the thermal stability of the high-entropy oxides. As a result, the nanoporous structure can be preserved even after high temperature calcination (Fig. 2g). However, the pore structure of R-HEO disappears before the formation of the high-entropy oxide.

We prepared well-dispersed Pt nanoparticles (~2.58 nm) *via* the polyol method [25]. To construct efficient catalysts, these Pt nanoparticles were loaded onto both R-HEO and S-HEO supports by an impregnation technique. TEM images show that the Pt nanoparticles are uniformly distributed on the fiber surfaces (Figs. 3a and b). This behavior is attributed to the negative surface charge of the HEO supports and the positive charge of freshly formed Pt nanoparticles: electrostatic attraction enhances loading efficiency, while same-charge repulsion inhibits particle agglomeration [26].

To assess the sinter-resistance of Pt/HEO, thermal aging tests were carried out. Pt/S-HEO catalysts were exposed to air at 500 °C and 600 °C for 2 h. TEM analysis revealed that the average size of Pt nanoparticles stayed at 2.8 nm at 500 °C, with no elemental segregation (Figs. 3c–e and Fig. S8 in Supporting information). Significantly, ICP quantification showed a Pt retention of 54.3 % after aging at 600 °C (Fig. S9 in Supporting information). In contrast, after thermal aging in air at 500 and 600 °C for 2 h, TEM images of Pt/R-HEO displayed marked sintering of Pt nanoparticles (Figs. 3f–h). This extensive coalescence was ascribed to the inherently dense R-HEO support structure, which caused dual mass and heat transfer limitations. By comparison, the Pt/S-HEO system, with its hierarchically porous network and robust metal-support interactions, jointly facilitated reactant diffusion, effective heat dissipation, and stabilization of active sites. These synergistic effects accounted for the superior thermal resilience of Pt/S-HEO and offered a theoretical basis for designing high-entropy oxide-based catalysts rationally.

XPS investigation was conducted on Pt/S-HEO samples calcined at different temperatures to elucidate the deactivation mechanisms and account for their divergent catalytic behaviors after thermal treatment. Initially, the oxygen-vacancy concentration in Pt/S-HEO was 11.6 %, but it rose to 21.9 % after calcination at 500 °C, likely due to thermal oxygen desorption. It then decreased slightly upon further heating to 600 °C (Fig. 4a). For the support of catalysts, Co, Mn, Fe, and Cr oxidation states varied in concert with the oxygen-vacancy content. Co exhibited Co^{3+} (780.3 eV) and Co^{2+} (782.0 eV) species (Figs. 4b–e) [27]. After 500 °C treatment, the Co^{3+} fraction increased but then declined at 600 °C. Mn displayed a similar trend between Mn^{3+} and Mn^{4+}, with Mn^{3+} decreasing from 65.2 % to 63.7 % at 500 °C and then rising to 68.5 % at 600 °C [28].

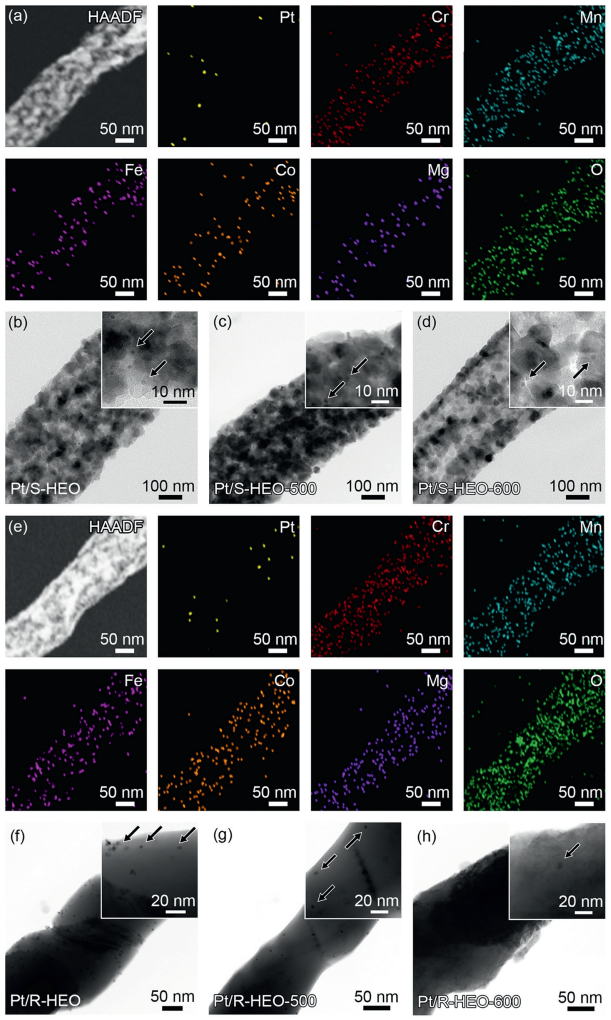


Fig. 3. (a) HAADF–STEM image and corresponding elemental mappings of Pt/S-HEO. The scale bars are 50 nm. TEM images of (b) Pt/S-HEO, (c) Pt/S-HEO-500, (d) Pt/S-HEO-600. (e) HAADF–STEM image and corresponding elemental mappings of Pt/S-HEO-500. The scale bars are 20 nm. TEM images of (f) Pt/R-HEO, (g) Pt/R-HEO-500, and (h) Pt/R-HEO-600.

In contrast, Fe showed an inverse behavior: The Fe^{2+} $2p_{3/2}$ peak at 710.4 eV grew at 500 °C before diminishing at 600 °C, whereas Fe^{2+} (712.7 eV) followed the opposite course [29]. Cr peaks at 576.3 eV (Cr^{3+}) and 578.8 eV (Cr^{6+}) revealed a maximum Cr^{6+} content of 30.3 % after 500 °C calcination [27]. Mg remained as Mg^{2+} throughout, underscoring its stabilizing role (Fig. 4f).

The Pt 4f core level reveals three major components: Pt^0, Pt^{2+}, and Pt^{4+}. In the Pt/S-HEO, the distribution is 69.4 % Pt^0, 25.0 % Pt^{2+}, and 5.6 % Pt^{4+}, corresponding to metallic Pt clusters and ionic interfacial species interacting with the HEO (Fig. 4g and Fig. S10 in Supporting information). Both Pt^{2+} and Pt^{4+} species increased after 500 °C treatment, attributable to decomposition of the PVP capping layer and the formation of strong chemical bonds at newly exposed Pt/HEO interfaces and between Pt and chemisorbed oxygen. At 600 °C, all Pt was found as Pt^{4+}. Notably, the Pt^{2+} peak shifted from 72.3 eV to 72.1 eV after 500 °C calcination, signaling electron transfer that strengthens metal–support interactions [30]. The rise in Pt^{2+} content after 500 °C air treatment is attributed to the formation of Pt–O–M (M = Cr, Mn, Fe, Co, Mg) linkages on the Pt/S-HEO surface; these Pt–oxygen bonds resist reduction even under high-temperature reducing conditions, further demonstrating the robust chemical coupling between Pt and the HEO support. *In situ*

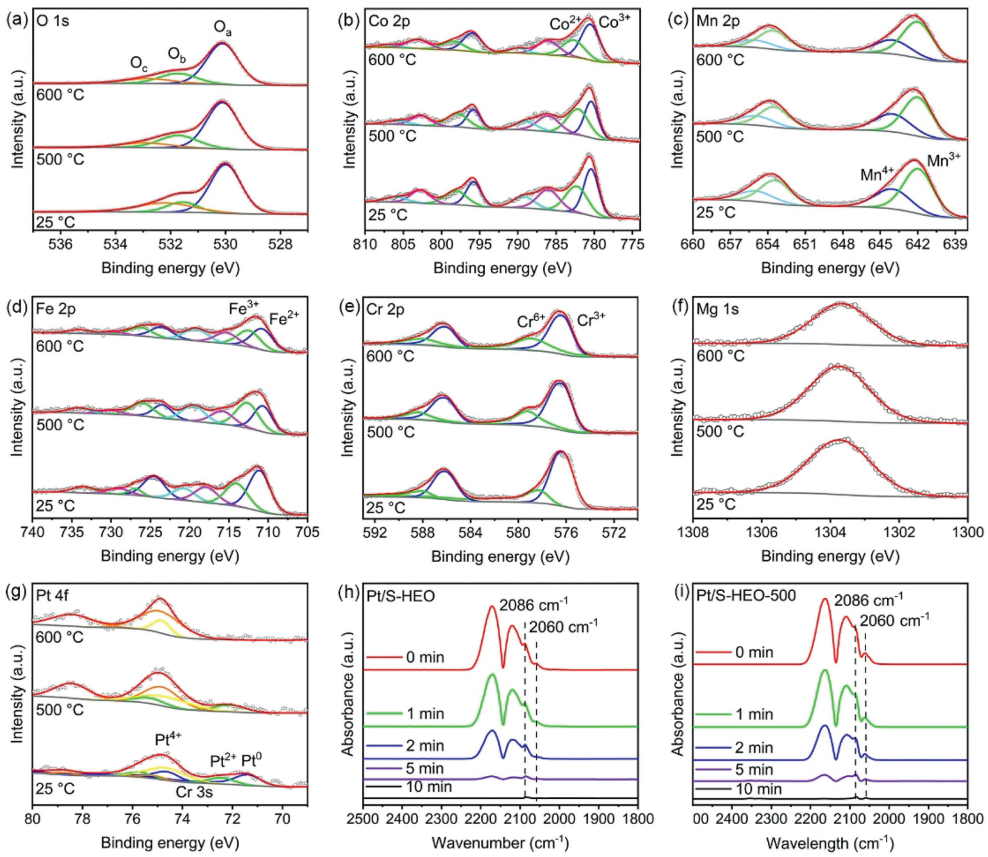


Fig. 4. XPS spectra of (a) O 1s, (b) Co 2p, (c) Mn 2p, (d) Fe 2p, (e) Cr 2p, (f) Mg 1s, (g) Pt 4f of Pt/S-HEO at elevated temperatures. *In situ* DRIFTS spectra of the CO desorption for (h) Pt/S-HEO and (i) Pt/S-HEO-500.

DRIFTS measurement with CO adsorption was used to investigate the Pt active sites in the catalysts. The peaks at 2171 and 2116 cm^{-1} are attributed to gaseous CO (Fig. S11 in Supporting information) [31]. The peak at 2062 cm^{-1} corresponds to undercoordinated edge sites characteristic of large Pt nanoparticles, whereas the peak at 2086 cm^{-1} originates from more terrace sites exposed on small Pt nanoparticles (Figs. 4h and i) [32]. Pt/S-HEO-500 still has a peak at 2086 cm^{-1}, after calcination at 500 °C. This behavior demonstrates the sinter-resistance of Pt nanoparticles.

The reduction process of the Pt/S-HEO was investigated using H_2-TPR. As shown in Fig. S12 (Supporting information), a strong peak appears at 262 °C, indicating the reduction of $Pt^{\delta+}$ to Pt^0 [33]. At 508 °C, a subsequent peak suggests possible re-oxidation of Pt to $Pt^{\delta+}$ [34]. The peak at 682 °C is attributed to the reduction of the surface shell or bulk phase of metal oxides, commonly linked to the reduction of support at high temperatures. The variation in hydrogen consumption peaks suggests that Pt nanoparticles interact with the S-HEO support *via* a hydrogen spillover effect, facilitating the reduction process of the support and thereby further enhancing the catalytic performance.

CO, a typical asphyxiant pollutant, poses significant environmental and human health risks due to its colorless and odorless nature. Primary emission sources encompass mobile sources (vehicle exhaust), stationary sources (industrial furnaces), and incomplete fossil fuel combustion processes, which collectively exacerbate atmospheric pollution. Consequently, the development of environmentally benign CO purification technologies has emerged as a global priority. Among various purification strategies, catalytic oxidation stands out as the most promising solution due to its energy efficiency and high effectiveness. These attributes drive the design of advanced catalysts, particularly nanostructured materials with high activity and thermal stability, representing a cutting-edge research focus in catalysis [35].

This study systematically investigates the thermal evolution and stabilization mechanisms of Pt/S-HEO and Pt/R-HEO catalysts under high-temperature CO oxidation conditions. Through thermal treatment experiments (500–600 °C) under oxygen-rich reaction conditions ($CO:O_2 = 1:5$), we elucidated the unique structural stability of HEO-based catalysts. The complete conversion temperature of S-HEO and R-HEO nanofibers in CO oxidation is approximately 400 °C (Fig. S13 in Supporting information), which highlights the synergistic effect by Pt nanoparticles and HEO supported [36]. Experimental results demonstrate that Pt/S-HEO exhibits exceptional stability. After aging at 500 °C, its T_{50} (temperature for 50 % CO conversion) increases by only 9 °C. Even at 600 °C, the T_{50} shift remains limited to 38 °C, significantly outperforming conventional catalyst systems (Fig. 5a). This remarkable thermal stability arises due to the synergistic stabilization effects of the HEO matrix. The slow diffusion effect from multicomponent interactions effectively suppresses Pt particle migration and sintering. Meanwhile, the strong metal-support interaction enhances the anchoring of active sites, thereby maintaining high dispersion under thermal stress. The Pt/S-HEO exhibited strong tolerance to vapor. When approximately 0.5 vol% vapor was introduced, only a negligible performance loss was observed, indicating excellent stability under humid conditions. The Pt/S-HEO calcined at 500 °C reached 100 % CO conversion at 215 °C with vapor, only 5 °C higher than that of the Pt/S-HEO-500 without vapor. These results emphasize the catalytic durability of the Pt/S-HEO system under hydrothermal conditions. In stark contrast, Pt/R-HEO suffers substantial performance degradation post 600 °C calcination, with its T_{50} increasing from 239 °C to 299 °C and T_{100} rising by 78 °C. For Pt/S-HEO, the T_{50}

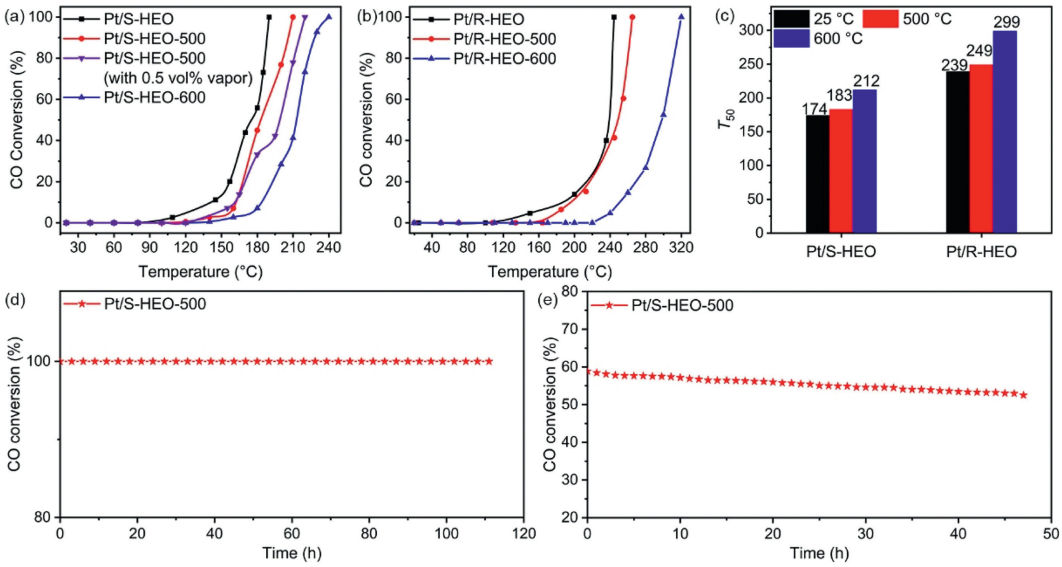


Fig. 5. CO oxidation performance of (a) Pt/S-HEO and (b) Pt/R-HEO at elevated temperatures. (c) T_{50} of Pt/S-HEO and Pt/R-HEO at elevated temperatures. (d, e) The stability of Pt/S-HEO-500.

increases only moderately from 174 °C to 212 °C, further confirming its superior thermal stability compared to Pt/R-HEO (Figs. 5b and c). This disparity is attributed to the dense microstructure of the R-HEO, which severely impedes mass transport and reaction kinetics.

Moreover, we conducted a systematic assessment of the long-term durability of Pt/S-HEO after 500 °C aging. As shown in Fig. 5d, the catalyst maintained 100 % CO conversion over 100 h of continuous reaction, demonstrating exceptional sinter resistance and extended operational lifetime (Table S1 in Supporting information). The catalyst exhibited merely a marginal activity decline of 6.3 % after continuous operation for 47 h, corresponding to a low deactivation rate constant of 6.5×10^{-3} h^{-1} (Fig. 5e and Table S2 in Supporting information). The hierarchically porous structure of the support not only provides abundant active sites but also physically restrains Pt nanoparticles, preventing their agglomeration or deactivation [37,38]. Meanwhile, we conducted TEM analysis after 47 h reaction. The results confirmed the exceptional thermal stability of the catalyst, with only a minimal increase of 0.13 nm (Fig. S14 in Supporting information). TEM images revealed that the pore structure of Pt/S-HEO-500 remained intact, showing no significant deterioration after the long-term reaction. This durability test further confirms the superior thermal and oxidative stability of the Pt/S-HEO. Collectively, these results underscore the robust structural integrity and functionality of Pt/S-HEO under high-temperature reaction conditions, highlighting its promise for industrial high-temperature catalytic applications.

For a fair contrast, we also compared the performance of Pt/S-HEO with Pt/Al_2O_3. Al_2O_3 nanofibers were prepared *via* electrospinning, followed by the impregnation method for loading Pt nanoparticles (Fig. S15 in Supporting information). After aging at 500 °C, the size of Pt nanoparticles on the Al_2O_3 nanofibers increased significantly from 2.6 nm to 3.9 nm (Fig. S16 in Supporting information). CO oxidation performance tests showed a marked degradation in both activity and stability. The T_{100} for CO oxidation over the Pt/Al_2O_3–500 increased by 45 °C after aging (Fig. S17 in Supporting information). Additionally, under prolonged testing at 56 % CO conversion, the catalytic activity decreased by 17.6 % within 10 h (Fig. S18 in Supporting information). The deactivation rate constant of Pt/Al_2O_3 was 0.07 h^{-1}, which is higher than that of Pt/S-HEO (6.5×10^{-3} h^{-1}). These results underscore the inherent instability of Pt/Al_2O_3, contrasting with the superior catalytic durability observed in Pt/S-HEO.

In this work, porous spinel type and rock-salt type high-entropy oxide nanofibers were fabricated *via* electrospinning, and the thermal stability of porous structures was systematically investigated. The high configurational entropy inherent in S-HEO induces the slow diffusion effect, which stabilizes their nanoporous architecture and enables retention of porosity up to 880 °C. In contrast, the R-HEO undergoes premature void collapse prior to achieving single-phase formation, consequently compromising its structural robustness. Upon exposure to thermal aging at 500 °C, the Pt nanoparticles on S-HEO exhibit a controlled increase in size, reaching an average dimension of 2.8 nm, underscoring the remarkable stability imparted by the high-entropy oxide support. In CO oxidation evaluations, the Pt/S-HEO-500 demonstrated great thermal stability, evidencing a mere 9 °C increase in T_{50} relative to the pristine Pt/S-HEO. Particularly, after aging at 500 °C, the Pt/HEO maintained its full CO conversion for over 100 h without any decline. Moreover, under continuous operation at 59 % CO conversion for 47 h, Pt/S-HEO-500 exhibited exceptional thermal stability with a low deactivation rate constant of 6.5×10^{-3} h^{-1}. These findings provide new insights for the rational design of high-temperature sintering-resistant catalysts and hold significant implications for the industrial application of noble-metal catalysts.

Declaration of competing interest

The authors declare that they have no known competing financial interests or personal relationships that could have appeared to influence the work reported in this paper.

CRediT authorship contribution statement

Yunpeng Wang: Writing – original draft, Visualization, Investigation. **Zhuxin Lyu:** Software, Investigation. **Yueming Sun:** Supervision, Project administration. **Yunqian Dai:** Writing – review & editing, Supervision, Funding acquisition, Conceptualization.

Acknowledgments

This work was financially supported by the National Key Research and Development Program of China (No. 2022YFA1505700),

the National Natural Science Foundation of China (No. 22475044), the Project of Qinglan Talent of Jiangsu, Pre-Research Fund of Ministry of Education of China (No. 8091B022212) and the Postgraduate Research & Practice Innovation Program of Jiangsu Province (No. KYCX22_0261).

Supplementary materials

Supplementary material associated with this article can be found, in the online version, at doi:10.1016/j.cclet.2025.112114.

References

[1] S. Cao, P. Rathi, X. Wu, et al., Adv. Mater. 33 (2021) e2000922.
[2] D. Liu, J. Liu, M. Yang, et al., Nano Energy 88 (2021) 106303.
[3] Q. Li, Q. Li, Z. Wang, et al., Small 20 (2024) e2303473.
[4] A. Wang, Y. Ma, D. Zhao, et al., ACS Nano 18 (2024) 22829–22854.
[5] M.J. Wang, J. Yang, L. Peng, et al., Chin. Chem. Lett. 35 (2024) 110573.
[6] Y. Zhang, S. Liu, J. Yan, et al., Adv. Mater. 33 (2021) e2105011.
[7] Y.F. Meng, Y.B. Zhu, L.C. Zhou, et al., Adv. Mater. 34 (2022) e2108267.
[8] W. Yuan, D. Zhang, Y. Ou, et al., Angew. Chem. Int. Ed. 57 (2018) 16827–16831.
[9] C. Zhang, Z. Wang, X. Wang, et al., Chin. Chem. Lett. 35 (2024) 110551.
[10] J. Zhao, J. Bao, S. Yang, et al., ACS Catal. 11 (2021) 12247–12257.
[11] C.M. Rost, E. Sachet, T. Borman, et al., Nat. Commun. 6 (2015) 8485.
[12] S. Akrami, P. Edalati, M. Fuji, et al., Mat. Sci. Eng. R. 146 (2021) 100644.
[13] H. Xu, Z. Zhang, J. Liu, et al., Nat. Commun. 11 (2020) 3908.
[14] M. Li, M. Song, W. Ni, et al., Chin. Chem. Lett. 34 (2023) 107571.
[15] L. Zhang, J. Jia, J. Yan, et al., Small 20 (2024) 2309586.
[16] J. Zou, L. Tang, W. He, et al., ACS Nano 18 (2024) 34492–34530.
[17] C. Triolo, K. Moulaee, A. Ponti, et al., Adv. Funct. Mater. 34 (2024) 2306375.
[18] Y. Wang, W. Xu, X. Zou, et al., J. Mater. Chem. A 11 (2023) 7422–7431.
[19] P. Feng, K. Dong, Y. Xu, et al., Adv. Fiber Mater. 6 (2024) 810–824.
[20] F. Sánchez-Bajo, F.L. Cumbrera, J. Appl. Crystallogr. 30 (1997) 427–430.
[21] Y. Han, J. Zou, Z. Li, et al., ACS Nano 12 (2018) 4835–4843.
[22] J. Wang, S. Liu, M. Tang, et al., Small 19 (2023) e2300547.
[23] X. Meng, X. Wang, K. Yin, et al., Proc. Natl. Acad. Sci. U. S. A. 121 (2024) e2317192121.
[24] C. Oses, C. Toher, S. Curtarolo, Nat. Rev. Mater. 5 (2020) 295–309.
[25] W. Fu, Y. Yu, K. Yin, et al., ACS Appl. Mater. Inter. 16 (2024) 47513–47523.
[26] W. Fu, K. Yin, Z. Li, et al., Chem. Sci. 15 (2024) 16688–16697.
[27] M.C. Biesinger, B.P. Payne, A.P. Grosvenor, et al., Appl. Surf. Sci. 257 (2011) 2717–2730.
[28] G. Fang, W. Chen, H. Yang, et al., Chin. Chem. Lett. 35 (2024) 108799.
[29] T.X. Nguyen, J. Patra, J.K. Chang, et al., J. Mater. Chem. A 8 (2020) 18963–18973.
[30] W. Xiao, Y. Chen, Q. Zhao, et al., Chin. Chem. Lett. 35 (2024) 110176.
[31] W. Wu, J. Luo, J. Zhao, et al., Nat. Commun. 15 (2024) 6108.
[32] Y. Xie, X. Yang, Z. Li, et al., Adv. Funct. Mater. (2025) 2505879.
[33] Y. Bai, H. Wang, C. Jin, et al., Appl. Catal. B: Environ. Energy 378 (2025) 125604.
[34] W. Li, Y. Guo, Y. Liu, et al., Vacuum 225 (2024) 113265.
[35] X. Tang, J. Wang, Y. Ma, et al., Chin. Chem. Lett. 32 (2021) 48–52.
[36] H. Chen, J. Fu, P. Zhang, et al., J. Mater. Chem. A 6 (2018) 11129–11133.
[37] Z. Deng, Y. Peng, W.W. Qin, et al., Chem. Eng. J. 475 (2023) 146260.
[38] Y. Li, B. Han, F. Bi, et al., ACS Appl. Mater. Interfaces 16 (2024) 66108–66116.